Supplementary Information

Programmable photoresponsive materials based on a single molecule via distinct topochemical reactions

Xiao Wei, Bao Li, Zhiqiang Yang, Ronglin Zhong, Yufei Wang, Yanan Chen, Zeyang Ding, Guangwen Men, Zairan Yang, Houyu Zhang, Bing Yang, Weiqing Xu and Shimei Jiang*

State Key Laboratory of Supramolecular Structure and Materials, College of Chemistry, Jilin University, 2699 Qianjin Street, Changchun 130012, P. R. China.

Table of Content

Methods

Preparation of BNA.

2-(3,5-bis (trifluoromethyl) phenyl) acetonitrile (1.39 g, 5.5 mmol) and 2-naphthaldehyde (0.78 g, 5.0 mmol) were added into 50 mL of ethanol. Pyrrolidine (0.70 g, 11.0 mmol) was dropped in the previous solution. Faint yellow product precipitated after stirring 12 h at room temperature. The product was collected through filtering and washing by ethanol to give a yellow solid (1.86 g, 95%). ^{1}H NMR (500 MHz, DMSO-d_6): δ/ppm = 8.59 (s, 1H), 8.51 (s, 1H), 8.43 (s, 2H), 8.22 (s, 1H), 8.19 (d, J = 8.7 Hz, 1H), 8.11 (d, J = 8.7 Hz, 1H), 8.02 (dd, J = 11.9, 8.6 Hz, 2H), 7.70 - 7.60 (m, 2H); ^{13}C NMR (126 MHz, DMSO-d6): δ/ppm = 107.66, 117.74,120.27, 122.44, 122.78, 124.61, 125.04, 126.68, 127.56, 128.17, 128.67, 129.09, 129.22, 131.12, 131.44, 131.71, 132.13, 132.88, 134.38, 137.02, 146.76; MS: m/z calculated for $C_{21}H_{11}F_6N$: 391.08; found 390.71.

Crystal growth

BNA was dissolved in dichloromethane to make a dilute solution. The green block crystals (**BNA-β**) were obtained with a slow evaporation rate at 16℃. To further tune molecular crystallization rate, a mixed solvent evaporation assembly method was employed for rapid crystallization. Ethanol as a poor solvent was injected into the dichloromethane solution of **BNA** to achieve the nearly saturated system. And then the needle-like crystals (**BNA-α**) quickly nucleated and precipitated in constant temperature water bath heating at 25℃.

Preparation of Adduct-α and Adduct-β.

The single crystals of **BNA-α** and **BNA-β** were ground into microcrystalline powders, and then these powders were spread into a 1 mm thin layers to receive irradiation with 365 nm OLED UV lamps (3.7 mW·cm^{-2}). The irradiated **BNA-α** (300 mg, 0.76 mmol)

was purified by column chromatography with hexane/dichloromethane mixture, 1:4 v/v, obtaining white solid **Adduct-α**. Yield: 204 mg, 0.26 mmol (68 %). The mixture of irradiated **BNA-β** (300 mg, 0.76 mmol) were purified by column chromatography with petroleum ether/dichloromethane mixture, 1:5 v/v, obtaining creamy white solid **Adduct-β**. Yield: 99 mg, 0.12 mmol (33 %). Purified **Adduct-α** and **Adduct-β** were dissolved in dichloromethane respectively, and their single crystals were formed after two or three days.

^{1}H NMR of **Adduct-α** (500 MHz, DMSO-d_6): δ/ppm = 8.22 (s, 2H), 8.09 (s, 2H), 8.04 (s, 4H), 7.92 – 7.90 (m, 2H), 7.885 (d, J = 8.7, 2H) 7.84 – 7.82 (m, 2H), 7.70 (dd, J = 8.7, 1.9 Hz, 2H), 7.58 – 7.54 (m, 4H), 6.49 (s, 2H).

^{1}H NMR of **Adduct-β** (500 MHz, DMSO-d_6): δ/ppm = 8.46 (s, 1H), 8.09 (s, 1H), 8.08 –8.05 (m, 3H), 7.98 – 7.93 (m, 4H), 7.9 (s, 2H), 7.63 (s, 1H), 7.54 (dt, J = 6.8, 3.4 Hz, 2H), 7.46 (d, J = 7.4 Hz, 1H), 7.33 (t, J = 7.5 Hz, 1H), 7.18 (t, J = 7.5 Hz, 1H), 6.87 (d, J = 7.6 Hz, 1H), 6.26 (s, 2H), 5.70 (d, J = 8.7 Hz, 2H).

Measurements.

^{1}H NMR and ^{13}C NMR spectra were recorded on a Bruker Advance 500 MHz spectrophotometer with tetramethylsilane (TMS) as the internal standard. Mass spectra was characterized by a Gas Chromatograph-Mass Spectrometer (GC-MS) (Thermo Fisher ITQ 1100^{TM}). The Powder X-ray diffraction (XRD) patterns were obtained with a Bruker D8 diffractometer with CuKα radiation (λ = 0.15418 nm). All PXRD results of samples are collected at room temperature. The crystal data and crystal face indices were collected on a Rigaku RAXIS-PRID diffractometer at ω-scan mode with monochromatized Mo Kα radiation (λ = 0.071073 nm). FTIR spectra were recorded with a Fourier transform infrared spectrometer (Bruker Optics VERTEX 80v). Morphology and photomechanical responses of crystal were performed with fluorescence microscopy (Vision Engineering Co., UK). Differential scanning calorimetry (DSC) was performed on a DSC Q20 instrument at a heating rate of 10

°C/min under a nitrogen purge. Thermogravimetric analysis (TGA) thermograms were obtained on a TA instrument at a heating rate of 10 °C/min under a nitrogen purge. Three-point bending tests of crystals were performed on INSTRON 9544 universal materials tester in the displacement control mode. Nanoindentation experiments were carried out on Nano Indenter G200 equipped with a Berkovich diamond tip with ~100 nm radius at a 0.1 mN/s loading rate. Mechanical behaviors of crystals were recorded by a Nikon Coolpix P7800 digital camera coupled to a reflectivity-mode optical microscope. UV/Vis absorption spectra were characterized by a UV/Vis spectrophotometer (Shimadzu UV-2600). Fluorescence spectra were measured by an optical fiber connected to Ocean Optics QE65 Pro spectrometer. The lifetime was collected on an Edinburgh FLS 980 spectrophotometer with TCPSC technology. A 365 nm OLED UV lamps (3.7 $mW \cdot cm^{-2}$) and a UV pulsed laser (under power of 10 $mW \cdot cm^{-2}$) with an optical fiber coupled were employed as light sources in this work. The OLED UV lamp was used to monitor the process of the photocycloaddition of **BNA** powders, and print different patterns on the fluorescent paper. The UV pulsed laser was used to test the photomechanical responses of **BNA** crystals at distance of 10 mm from, and write on the fluorescence paper.

Crystallographic data.

The single crystal date of **BNA-α**, **BNA-β**, **Adduct-α** and **Adduct-β** have been deposited as CIF files into Cambridge Crystallographic Data Center. The publication numbers CCDC is 2032920, 2113420, 2032927 and 2032930.

Theoretical calculation.

Density functional theory (DFT) and time-dependent density functional theory (TD-DFT) calculation were employed to explore the processes of fluorescence change. The geometries of the *π-dimers* were obtained from **BNA-α** and **BNA-β** crystals structures. The ground state geometries of **Adduct-α** and **Adduct-β** were subjected to optimized

by DFT computations of B3LYP/6-31G(d) in Gaussian 09 package; The excitation energies in the n-th singlet (*S*n) states were performed by TD-DFT computations of B3LYP/6-31G(d)**.**

The energy of **BNA** reactants and **Adduct-α** and **Adduct-β** products were treated by utilizing B3LYP level of theory with Pople 6-31G (d) basis set.

Fabrication of Photoactuator and Photoswitching.

Two crystals of **BNA-α** with different thickness were fixed on the left and right sides of a capillary tip with 502 glue. This micron optic-controlled tweezer was connected to a 3-dimensional operation platform to help it gain movement. When the light source on the side of the relatively thinner crystal was turned on, the distance between the two single crystals was reduced and the object could be picked up.

The **BNA** was dissolved in dichloromethane, after adding ethanol, the solution was stirred overnight. And then uniform **BNA-β** nanocrystals precipitated. The nanocrystals were evenly spread on the transparent adhesive tape to prepare rewritable fluorescent rewritable fluorescent for photoswitching.

Preparation and Characterization of BNA.

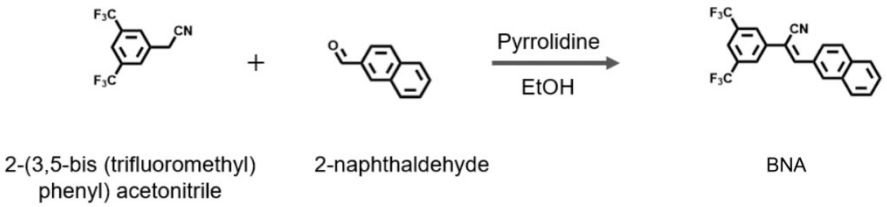

Scheme S1. Synthetic route of **BNA**.

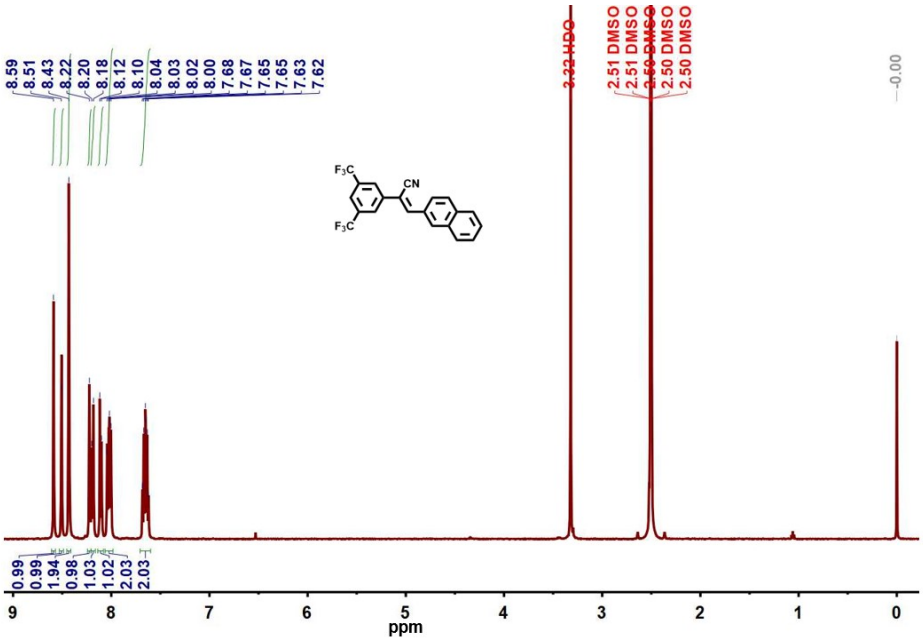

Figure S1. ^{1}H NMR spectrum of **BNA** in DMSO-d_6 (500 MHz).

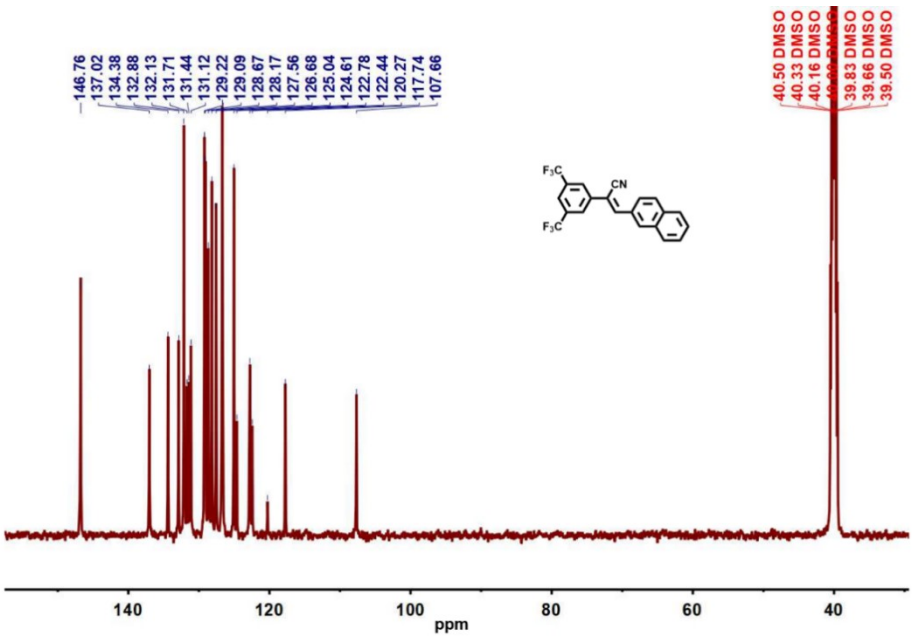

Figure S2. ^{13}C NMR spectrum of **BNA** in DMSO-d_6 (500 MHz).

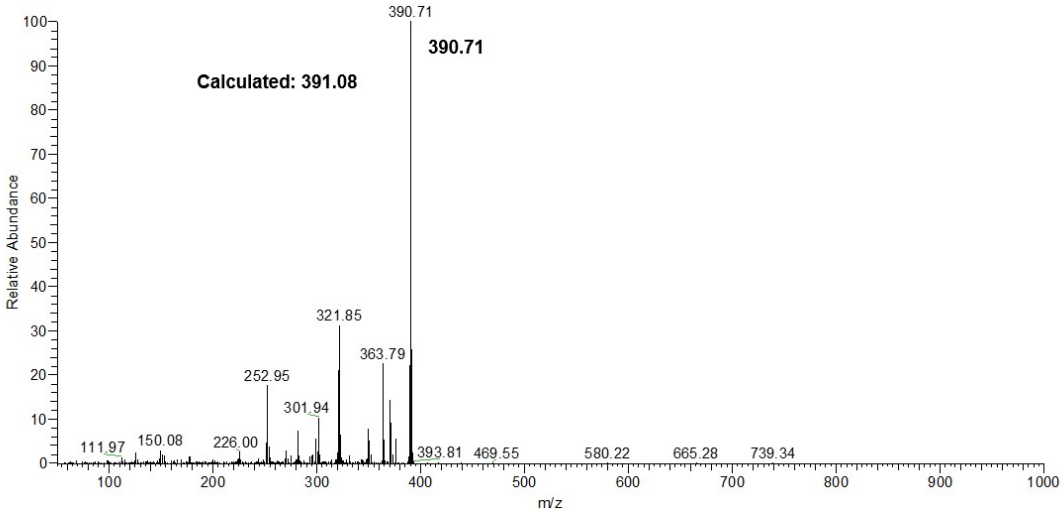

Figure S3. Mass spectrum of **BNA**.

Molecular Preorganization with Different Hierarchical Architectures.

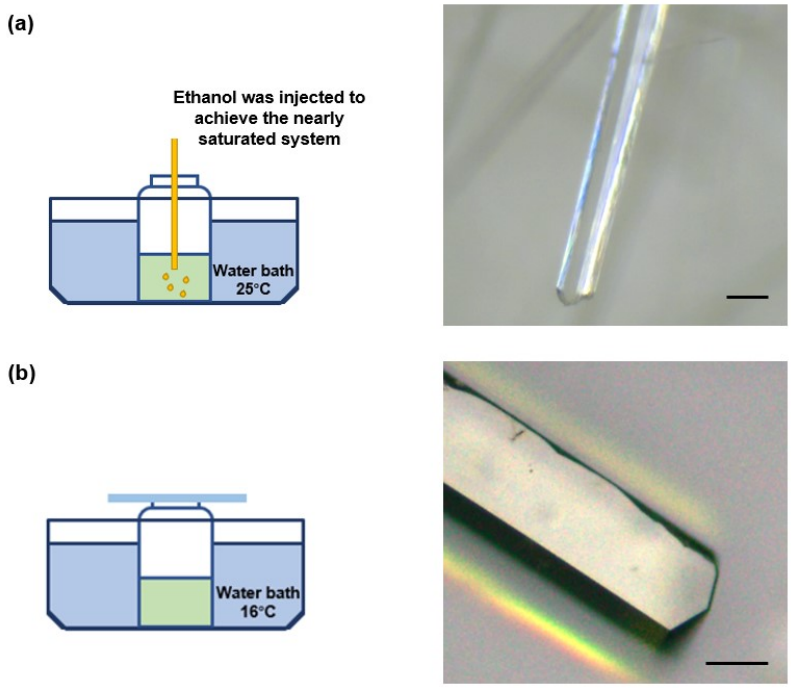

Figure S4. The schematic illustrations of the crystal growth and the optical micrographs of the single crystals taken under room light. (a) needle shape crystals (**BNA-α**) prepared by rapid evaporation from ethanol and dichloromethane mixed solution and (b) block shape crystals (**BNA-β**) prepared from dichloromethane solution in a relatively sealed system. The scale bar is 200 μm.

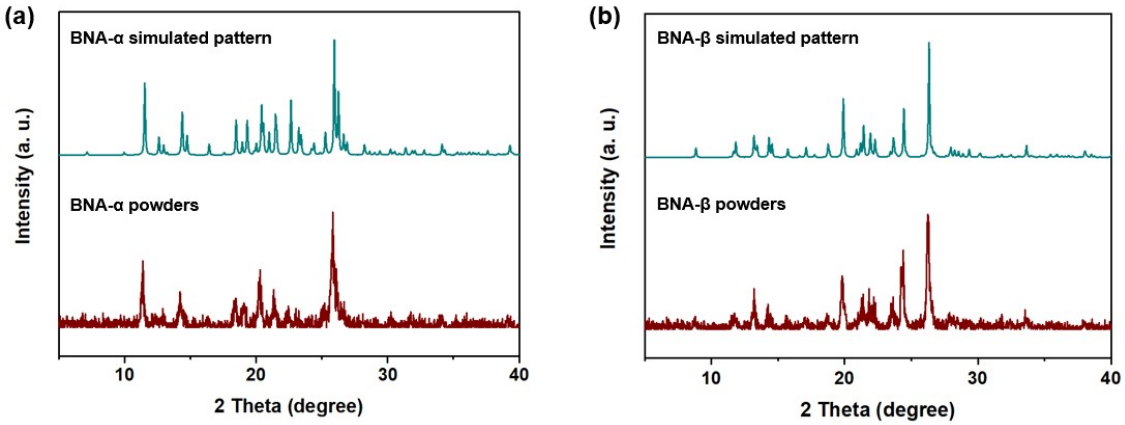

Figure S5. PXRD patterns of **BNA-α** and **BNA-β** powders.

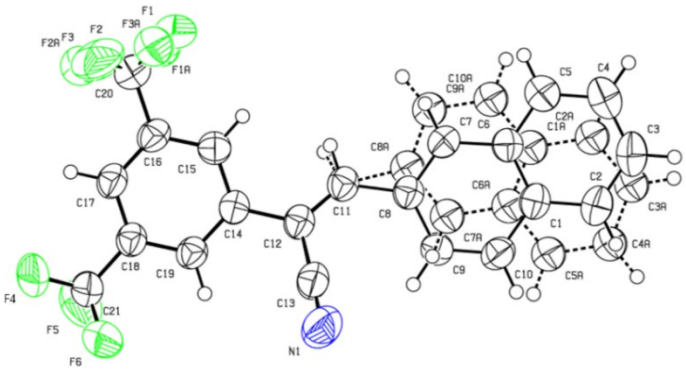

Figure S6. Thermal ellipsoid diagram of **BNA-α**.

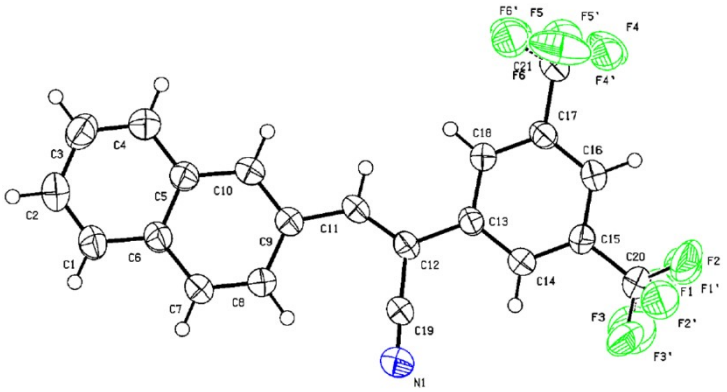

Figure S7. Thermal ellipsoid diagram of **BNA-β**.

Table S1. Crystal data and structure refinement for **BNA-α**.

Empirical formula	$C_{21}H_{11}F_6N$
Formula weight	391.31
Temperature (*K*)	99(2)
Crystal system	Triclinic
Space group	*P*-1
a (Å)	7.8885(8)
b (Å)	9.5215(10)
c (Å)	12.4914(13)
α (°)	94.944(4)
β (°)	94.830(4)
γ (°)	110.235(4)
Volume (Å^3)	870.50(16)
Z	2
d_{cal} (g cm^{-3})	1.493
μ (mm^{-1})	0.133
F (000)	396
Crystal size (mm^3)	0.130 × 0.120 × 0.100
Radiation	CuKα (λ = 1.54184)
θ range for data collection (°)	2.904 to 27.501
Index ranges	$-10 \le h \le 10$, $-12 \le k \le 12$, $-16 \le l \le 16$
Reflections collected	26410
Independent reflections	3988 [R_{int} = 0.0361]
Completeness to θ = 25.242°	99.8 %
Data / restraints / parameters	3988 / 0 / 259
Goodness-of-fit on F^2	1.024
Final *R* indices [$I > 2\sigma(I)$]	R_1 = 0.0536, wR_2 = 0.1274
R indices [all data]	R_1 = 0.0906, wR_2 = 0.1554
Largest diff. peak and hole (e Å^{-3})	0.292 and -0.206

Table S2. Crystal data and structure refinement for **BNA-β**.

Empirical formula	$C_{21}H_{11}F_6N$
Formula weight	391.31
Temperature (*K*)	293
Crystal system	monoclinic
Space group	*P* 1 21/*n* 1
a (Å)	8.4375(3)
b (Å)	15.1706(7)
c (Å)	13.3563(6)
α (°)	90
β (°)	96.315(2)
γ (°)	90
Volume (Å^3)	1699.23(13)
Z	4
d_{cal} (g cm^{-3})	1.530
μ (mm^{-1})	0.136
F (000)	792.60
Crystal size (mm^3)	0.110 × 0.100 × 0.100
Radiation	CuKα (λ = 1.54184)
θ range for data collection (°)	2.685 to 27.503
Index ranges	$-10 \le h \le 9$, $-19 \le k \le 19$, $-17 \le l \le 17$
Reflections collected	11085
Independent reflections	3894 [R_{int} = 0.0437]
Completeness to θ = 25.242°	99.9 %
Data / restraints / parameters	3894 / 0 / 279
Goodness-of-fit on F^2	1.019
Final *R* indices [$I > 2\sigma(I)$]	R_1 = 0.0685, wR_2 = 0.1792
R indices [all data]	R_1 = 0.1059, wR_2 = 0.2209
Largest diff. peak and hole (e Å^{-3})	0.424 and -0.270

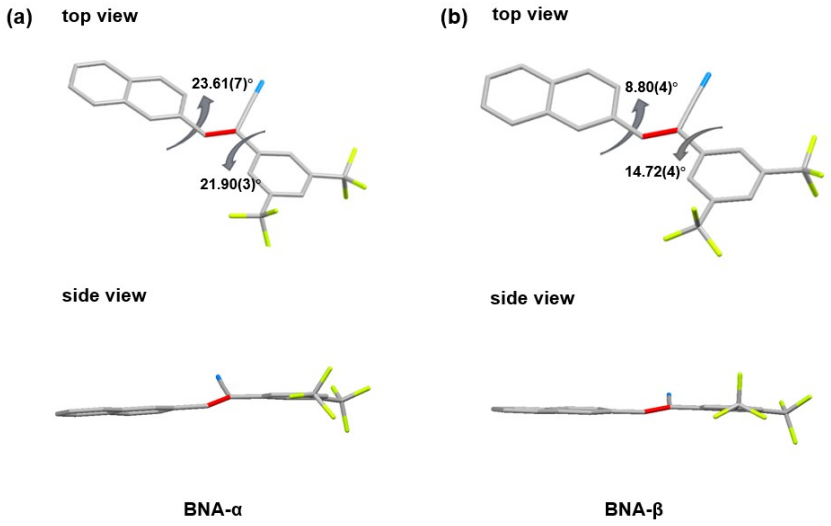

Figure S8. Molecular configurations in (a) **BNA-α** and (b) **BNA-β** single crystals.

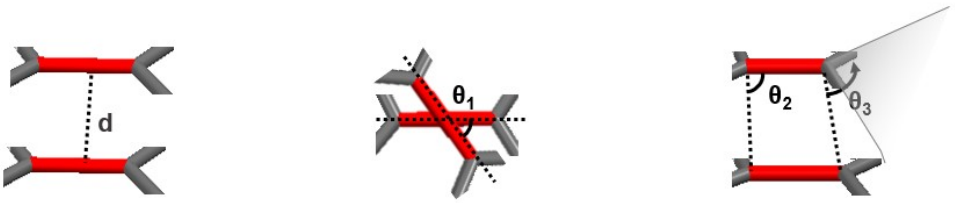

Figure S9. The parameters of geometric criteria within ***π-dimer***. The distance between the olefin units is required within 4.2 Å. The angles (θ1, θ2, and θ3) are used to judge the parallelism, and the ideal values are 0°, 90°, and 90°, respectively.

Table S3. Geometric parameters of **BNA-α** and **BNA-β** crystals.

	***d* (Å)**	**θ_1 (degree)**	**θ_2 (degree)**	**θ_3 (degree)**
BNA-α	3.607(3)	0.00(11)	86.95(16)	78.39(14)
BNA-β	3.651(4)	16.33(12)	100.29(18)	79.45(17)
Ideal	< 4.2	0	90	90

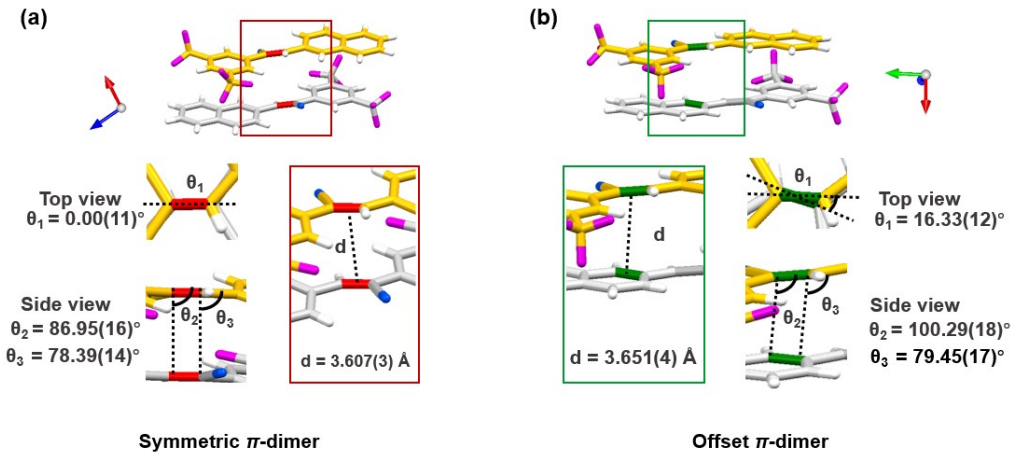

Figure S10. The *intra-π-dimer* structure of (a) **BNA-α** and (b) **BNA-β** single crystals.

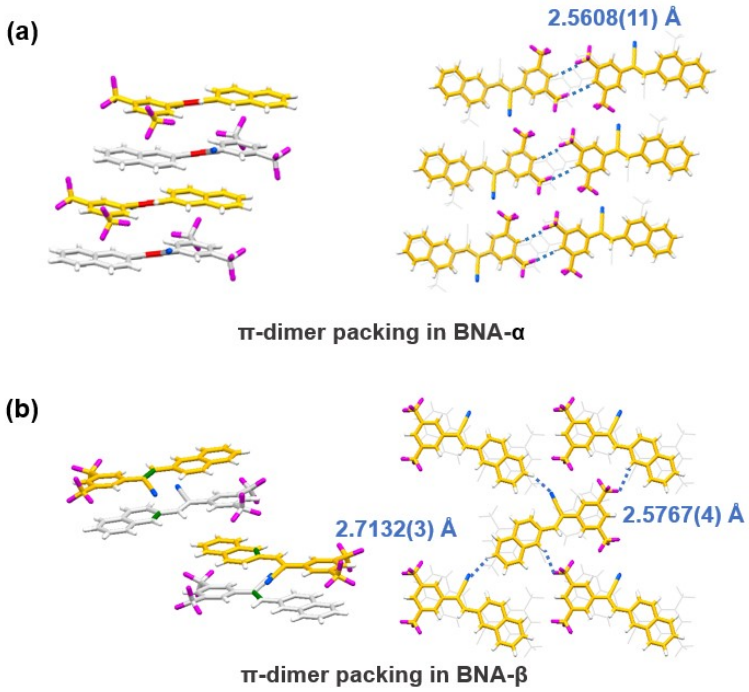

Figure S11. The *inter-π-dimer* packing in (a) **BNA-α** and (b) **BNA-β** single crystals.

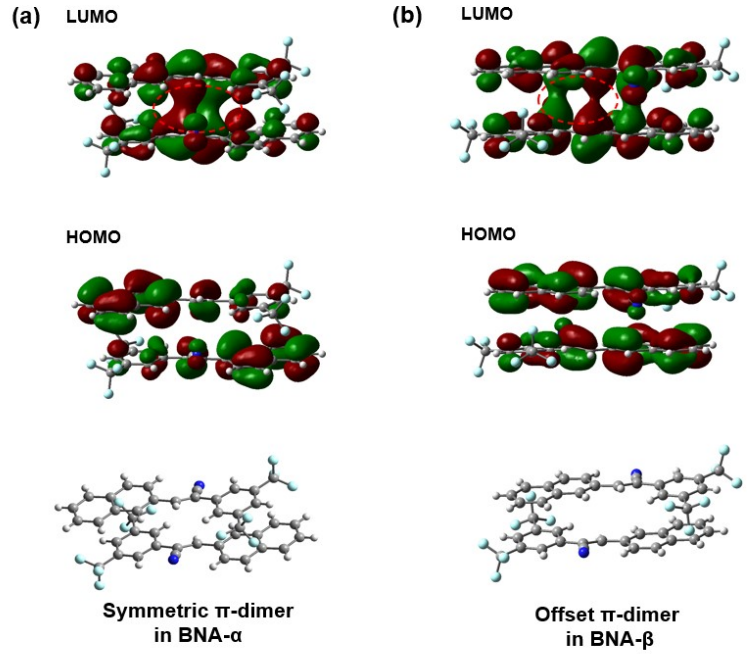

Figure S12. Theoretical calculation of **BNA** *π-dimer*. (a) In-phase interaction between the lowest unoccupied molecular orbitals (LUMOs) of C=C bond pairs in the symmetric *π-dimer* of **BNA-α**. (b) The overlapping between the LUMOs of olefin and aromatic ring in the offset *π-dimer* of **BNA-β** single crystals.

Characterization of Photocycloaddition Products.

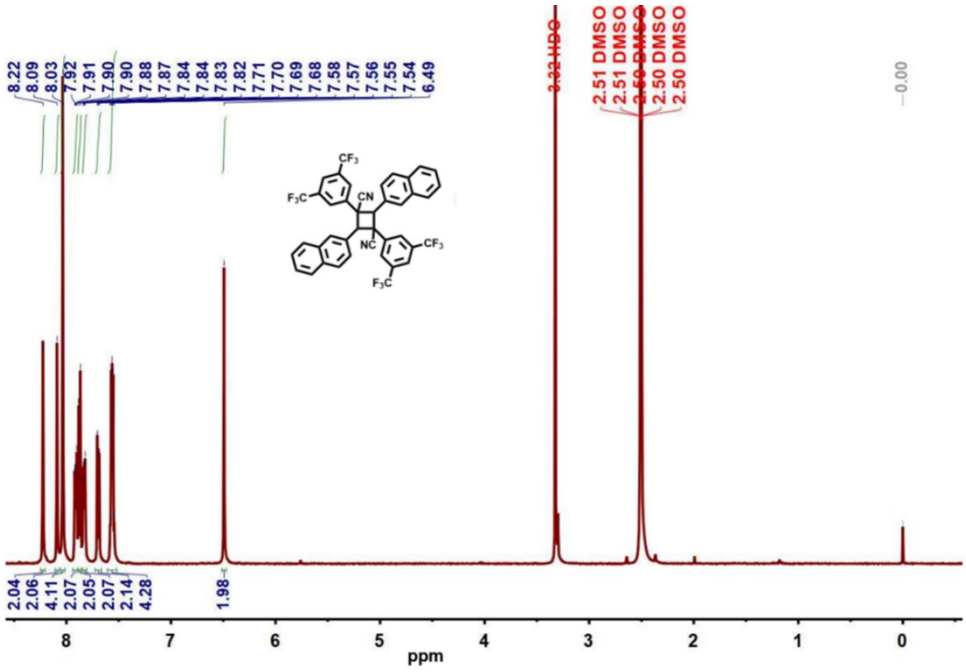

Figure S13. ^{1}H NMR spectrum of **Adduct-α** in DMSO-d_6 (500 MHz).

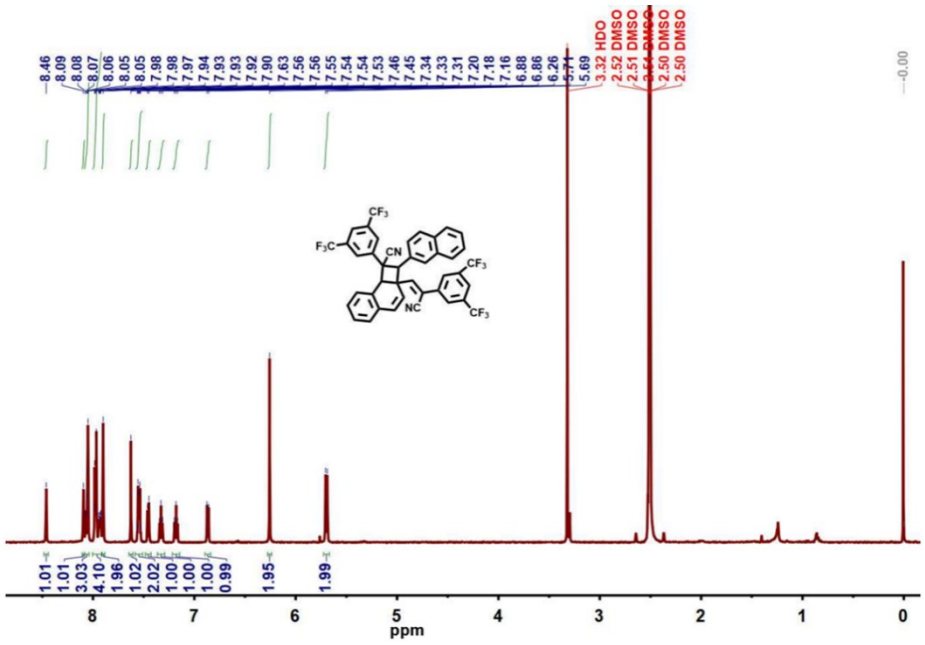

Figure S14. ^{1}H NMR spectrum of **Adduct-β** in DMSO-d_6 (500 MHz).

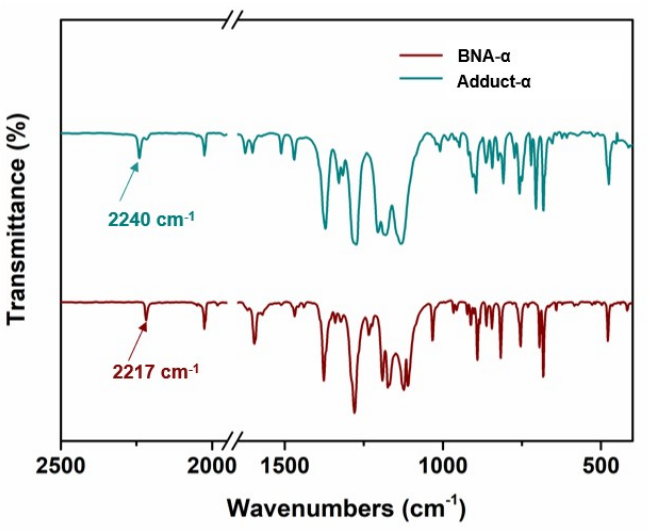

Figure S15. FT-IR spectra (KBr pellets) of **BNA-α** and **Adduct-α**.

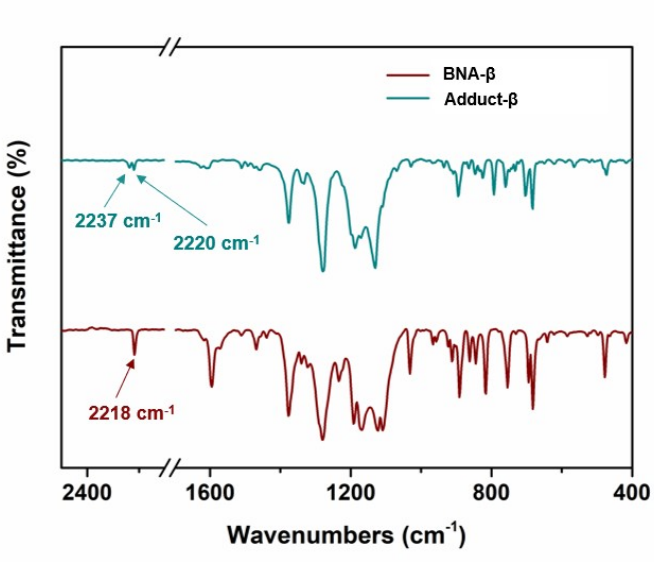

Figure S16. FT-IR spectra (KBr pellets) of **BNA-β** and the **Adduct-β**.

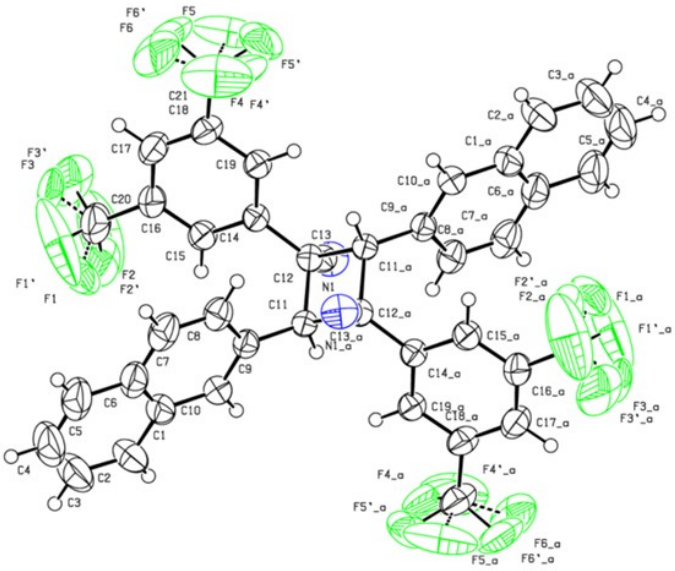

Figure S17. Thermal ellipsoid diagram of **Adduct-α**.

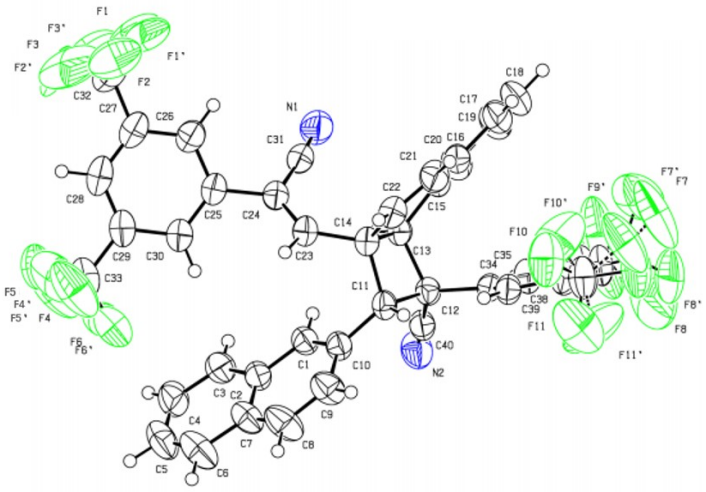

Figure S18. Thermal ellipsoid diagram of **Adduct-β**.

Table S4. Crystal data and structure refinement for **Adduct-α**.

Empirical formula	$C_{42}H_{22}F_{12}N_2$
Formula weight	782.61
Temperature (*K*)	98(2)
Crystal system	triclinic
Space group	*P*-1
a (Å)	6.6239(3)
b (Å)	11.3191(6)
c (Å)	12.9368(7)
α (°)	67.4855(17)
β (°)	84.6786(17)
γ (°)	89.830(2)
Volume (Å^3)	891.61(8)
Z	1
d_{cal} (g cm^{-3})	1.458
μ (mm^{-1})	0.129
F (000)	396
Crystal size (mm^3)	0.130 × 0.120 × 0.100
Radiation	CuKα (λ = 1.54184)
θ range for data collection (°)	3.050 to 25.730
Index ranges	$-8 \le h \le 8$, $-13 \le k \le 13$, $-15 \le l \le 15$
Reflections collected	27462
Independent reflections	3349 [R_{int} = 0.0539]
Completeness to θ = 25.242°	99.3 %
Data / restraints / parameters	3349 / 0 / 310
Goodness-of-fit on F^2	1.014
Final *R* indices [$I > 2\sigma(I)$]	R_1 = 0.0539, wR_2 = 0.1292
R indices [all data]	R_1 = 0.0789, wR_2 = 0.1448
Largest diff. peak and hole (e Å^{-3})	0.160 and -0.161

Table S5. Crystal data and structure refinement for **Adduct-β**.

Empirical formula	$C_{42}H_{22}F_{12}N_2$
Formula weight	782.61
Temperature (*K*)	293(2)
Crystal system	monoclinic
Space group	*P*2 (1) /*c*
a (Å)	16.3007(12)
b (Å)	18.4842(13)
c (Å)	12.5889(9)
α (°)	90
β (°)	90
γ (°)	109.832(3)
Volume (Å^3)	3568.1(4)
Z	4
d_{cal} (g cm^{-3})	1.457
μ (mm^{-1})	0.129
F (000)	1584
Crystal size (mm^3)	0.130 × 0.120 × 0.100
Radiation	CuKα (λ = 1.54184)
θ range for data collection (°)	2.736 to 26.376
Index ranges	$-20 \le h \le 20$, $-23 \le k \le 23$, $-15 \le l \le 15$
Reflections collected	53329
Independent reflections	7269 [R_{int} = 0.0472]
Completeness to θ = 25.242°	99.8 %
Data / restraints / parameters	7269 / 0 / 618
Goodness-of-fit on F^2	1.014
Final *R* indices [$I > 2\sigma(I)$]	R_1 = 0.0438, wR_2 = 0.1016
R indices [all data]	R_1 = 0.0786, wR_2 = 0.1256
Largest diff. peak and hole (e Å^{-3})	0.155 and -0.151

Thermodynamic Analysis of Irradiated BNA-α and BNA-β Samples.

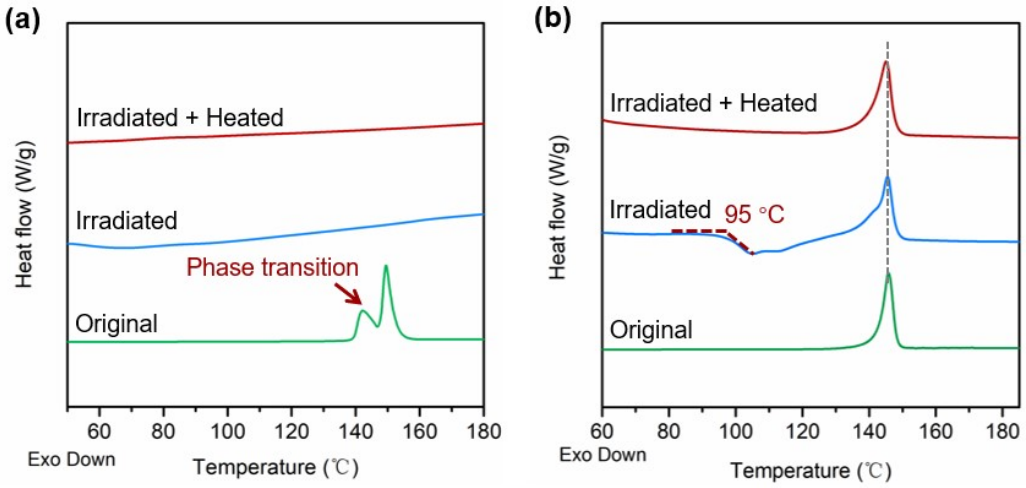

Figure S19. DSC curves of (a) **BNA-α** and (b) **BNA-β** in different states. Their curves demonstrate different thermal stabilities of the irradiated **BNA-α** and **BNA-β** powders. The irradiated **BNA-α** is stable and there is no thermal cleavage (retrocycloaddition) before 180°C. But the irradiated **BNA-β** exhibits poor stability, it can undergo thermal cleavage (retrocycloaddition) at 95°C.

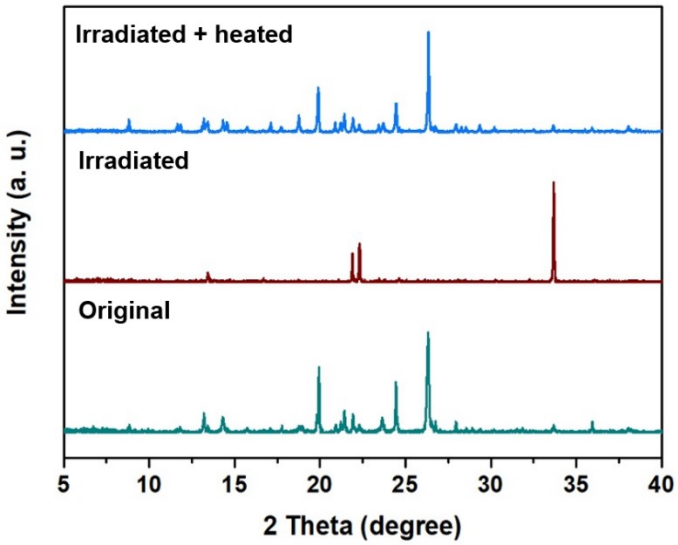

Figure S20. PXRD patterns of **BNA-β** in different states (The green, red and blue lines represent the original one, the one after irradiation and the heated one after irradiation, respectively.).

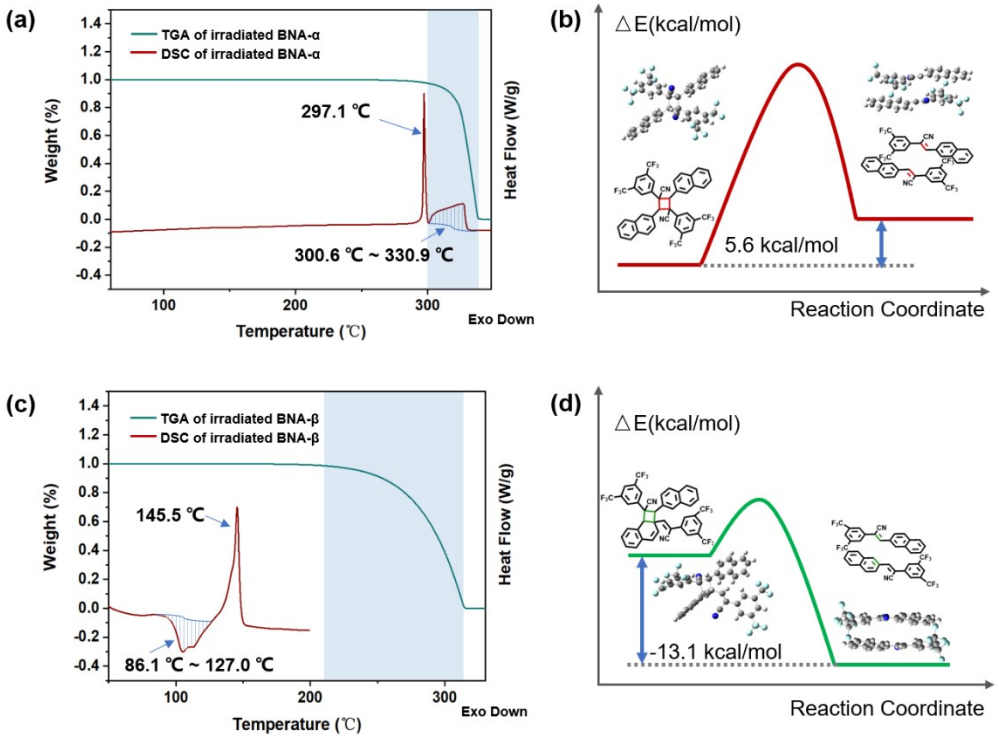

Figure S21. DSC and TGA thermogram of (a) irradiated **BNA-α** and (c) irradiated **BNA-β**. Energy profiles for (b) olefin-olefin [2+2] retrocycloaddition reactions and (d) olefin-aromatic ring [2+2] retrocycloaddition reactions.

For the DSC thermogram of irradiated **BNA-α** powders, following the melting endothermic peak of irradiated product (**Adduct-α**) at 297.1 °C, there is a broad endotherm (300.6 ~ 330.9 °C) that corresponds to a complete weight loss of the TGA thermogram (300.6 ~ 348.2 °C). This result indicates that the melted **Adduct-α** undergoes a decomposition and a evaporation of monomers during the broad endotherm process. The enthalpy (ΔH) that involves both decomposition and phase transition is calculated to be 32.15 kcal/mol by integrating the broad endothermic zone.

The energy profiles of olefin-olefin [2+2] retrocyloadditions in **BNA-α** powders demonstrate that the irradiated product **Adduct-α** is stable with lower energy. Gibbs free energies (ΔG_{cal}) of this retrocyloadditions is 5.6 kcal/mol. The enthalpy of this retrocyloadditions can calculated from $\Delta G_{cal} = \Delta H_{cal} - T\Delta S_{cal}$, where T is the absolute temperature, ΔS_{cal} (55.49 cal/mol) is provided from the theoretical calculation data.

ΔH_{cal} is calculated to be 22.1 kcal/mol. This value of ΔH_{cal} corresponds to the olefin-olefin [2+2] retrocyloadditions, which does not involve the phase transition. Therefore, the ΔH_{cal} from energy profiles is smaller than the ΔH from DSC thermogram.

For the DSC thermogram of irradiated **BNA-β** powders, there is a broad exothermic peak (86.1 ~ 127 °C). The results of ^{1}H NMR spectra proved that the irradiated **BNA-β** powders undergo retrocycloaddition during this exothermic process. Noting that the melting endothermic peak of monomer is at 145.5 °C, so the retrocycloaddition does not involve the phase transition. The enthalpy (ΔH) of retrocycloaddition is calculated to be -8.3 kcal/mol from the DSC thermogram. As shown in the energy profiles (Figure S21d), the irradiated product of **Adduct-β** has higher energy. ΔG_{cal} of olefin-aromatic [2+2] retrocyloadditions is -13.1 kcal/mol. According to the equation $\Delta G_{cal} = \Delta H_{cal} - T\Delta S_{cal}$, ΔH_{cal} is calculated to be -7.6 kcal/mol, which is consistent with the ΔH from DSC thermogram.

In summary, irradiated product **Adduct-α** with lower energy demonstrates better stability. It undergoes a decomposition and a evaporation of the corresponding monomers at a very high temperature with the absorption of energy. Whereas irradiated product **Adduct-β** in microcrystal powders has higher energy due to the involvement of aromatic ring. **Adduct-β** in irradiated microcrystal powders can be thermally cleaved to monomers at lower temperature with the release of energy.

Calculated Growth Morphology and Mechanics Tests.

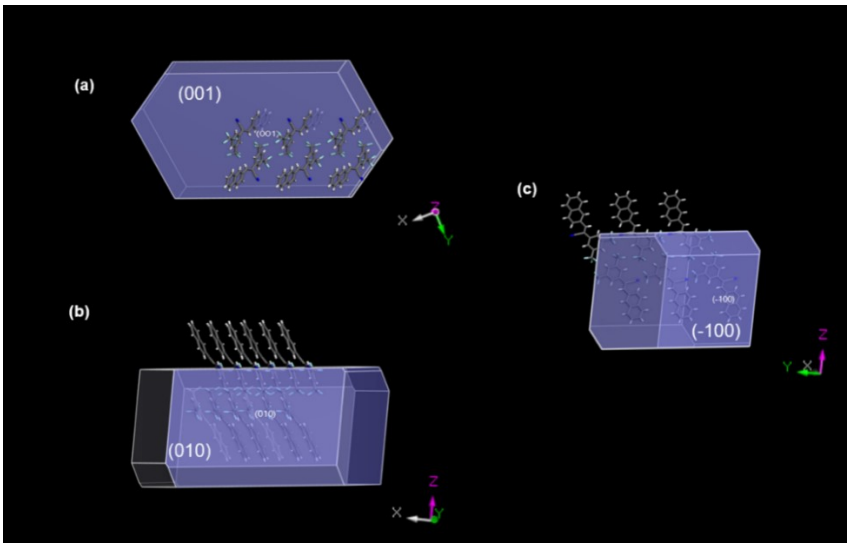

Figure S22. Calculated growth morphology of **BNA-α**.

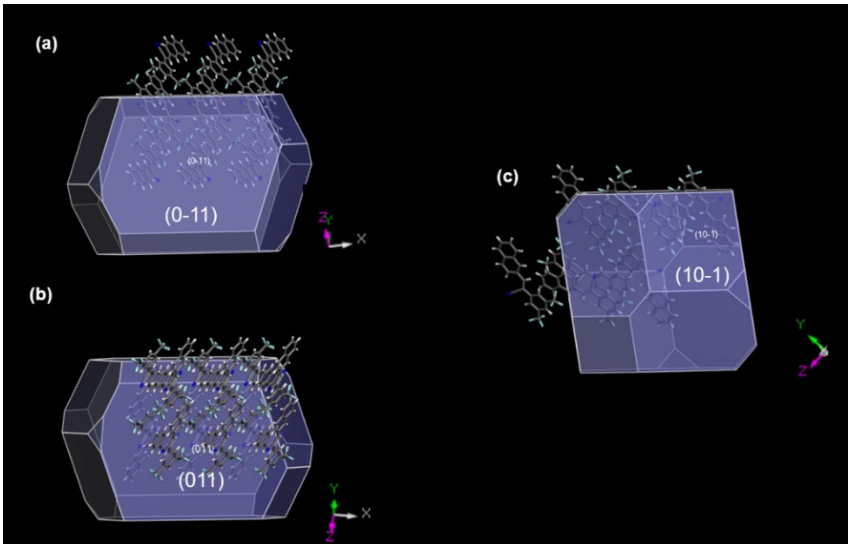

Figure S23. Calculated growth morphology of **BNA-β**.

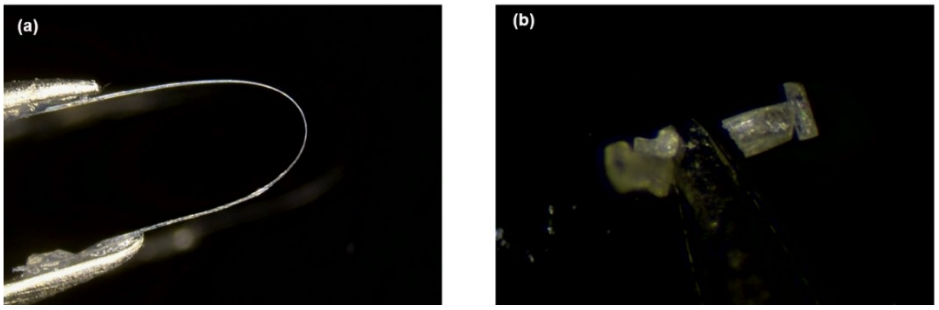

Figure S24. Crystal qualitative mechanics tests of (a) **BNA-α** and (b) **BNA-β** under mechanical stress applied through a pair of tweezers.

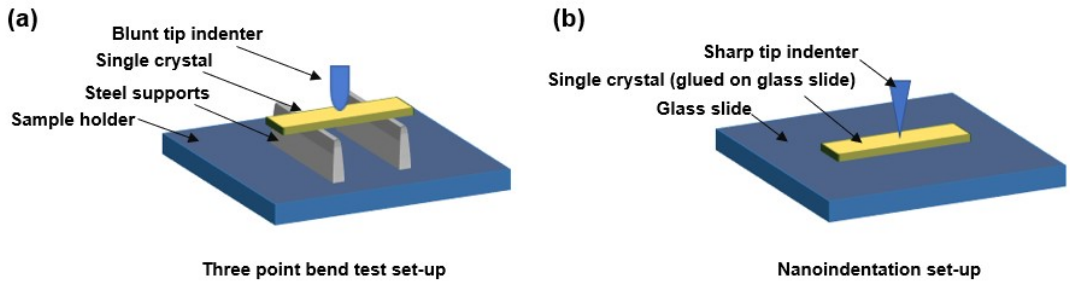

Figure S25. Schematic setup of three-point bending tests and nanoindentation tests.

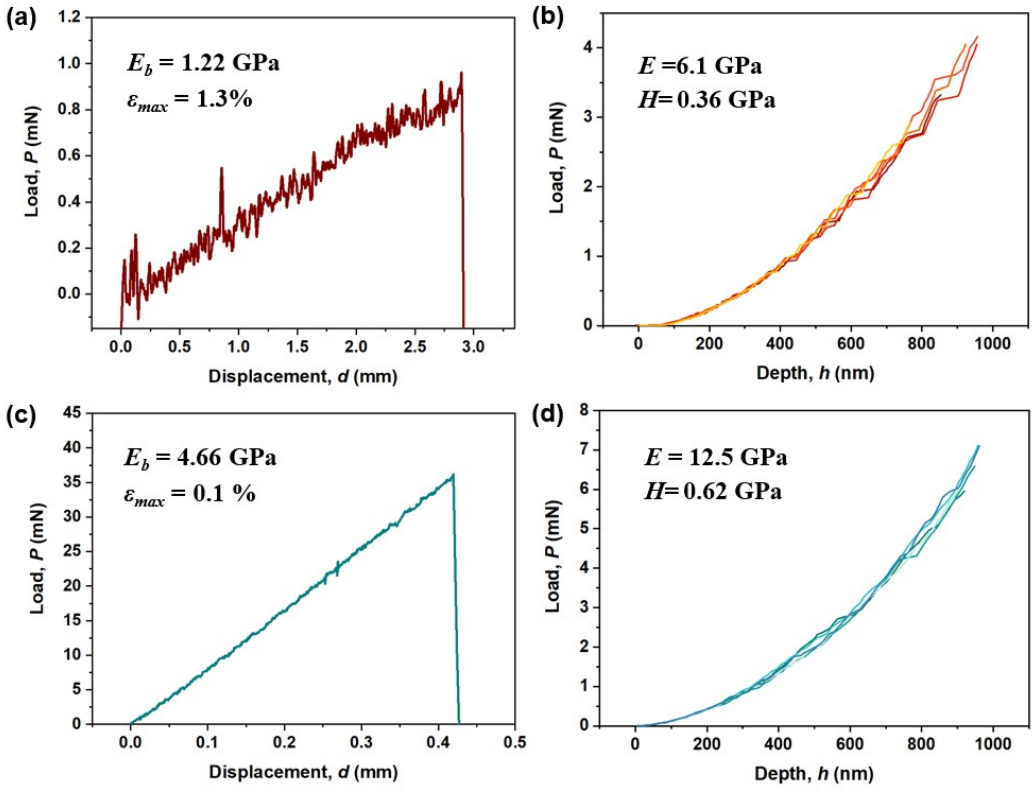

Figure S26. Crystal quantitative mechanics tests. Load–displacement (*P*–*d*) curve of (a) **BNA-α** and (c) **BNA-β** crystals obtained from three-point bending tests. Load–displacement (*P*–*h*) curves of (b) **BNA-α** and (d) **BNA-β** crystals obtained from the nanoindentation tests. Three-point bending tests of crystals were performed in the displacement control mode. The bending elastic modulus, E_b, were calculated with the equation $E_b = \frac{PL^3}{48I\delta}$, where P is the load applied at the center of the span length L, δ is the beam deflection at the center of span, and I is the area moment of inertia for a rectangular cross-section. The yield strain, ε_{max}, were calculated by using the equation

$\varepsilon_{max} = \frac{6\delta h}{L^2}$, where h is the thickness of materials. Nanoindentation experiments were utilized to measure the elastic modulus (E) and hardness (H) of crystals. The values of E_b, E *and* H of **BNA-β** crystals are higher than those of **BNA-α** crystals, indicating that **BNA-β** crystals is inflexible and hard. In addition, the ε_{max} of **BNA-β** crystals is much smaller than that of **BNA-α** crystals, which demonstrates that the **BNA-β** crystals is easier to be fractured under the external force.

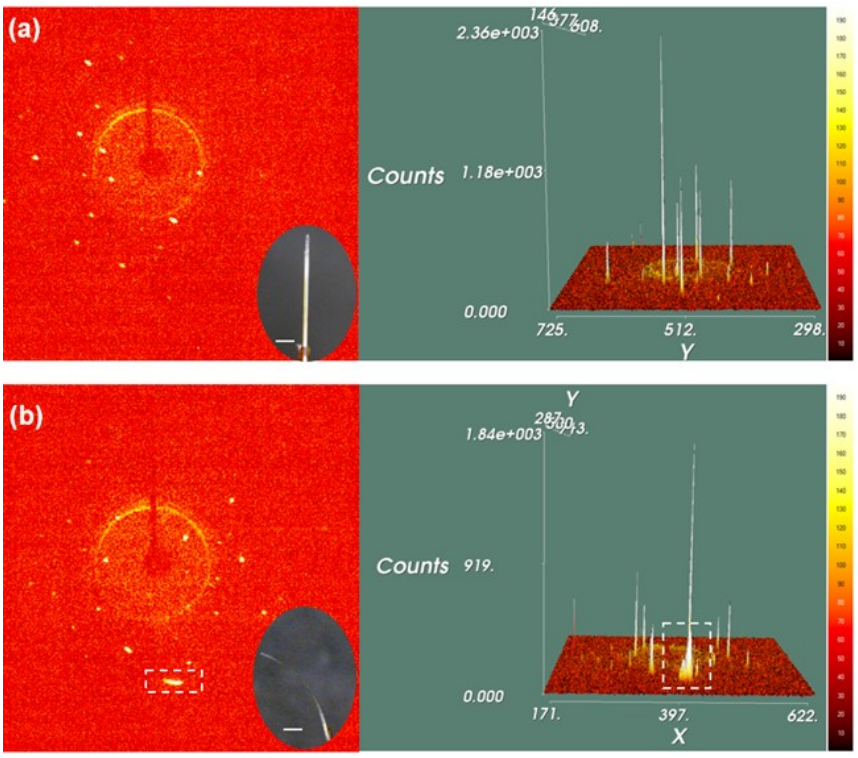

Figure S27. Bruker diffraction images of **BNA-α** crystal (a) before and (b) after UV irradiation. The area in (b) selected with white dotted line show a significant elongation of the diffraction spots, indicating the partially molecular displacement caused by [2+2] photocycloaddition reactions. The other diffraction spots in (b) with good shape demonstrated that the periodic nature of crystal was partly retained. The scale bar is 1 mm.

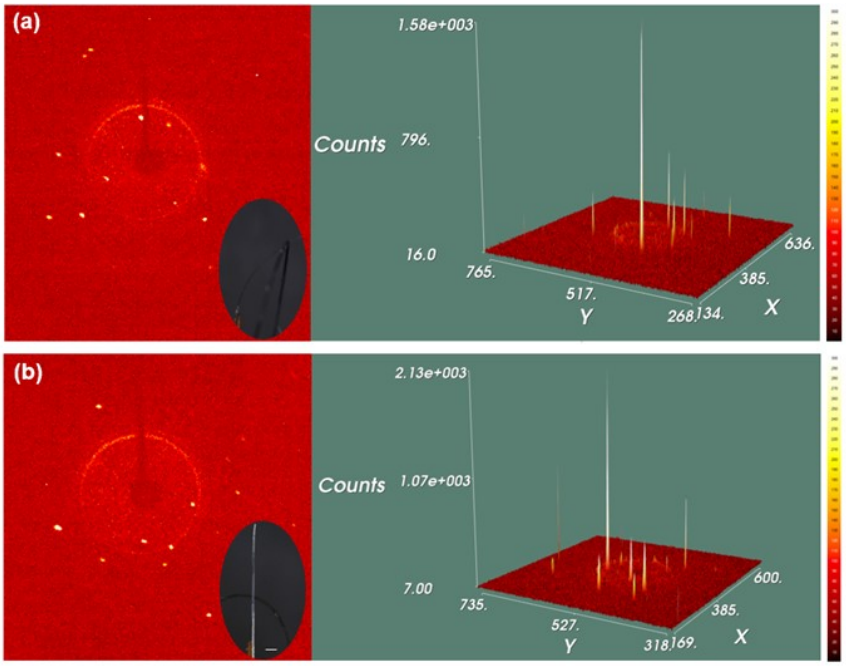

Figure S28. Bruker diffraction images of **BNA-α** crystal (a) bended by external force and (b) after the release of external force. Their diffraction spots with good shape and intensity demonstrated that the bent and recovered crystal also remained crystalline. The scale bar is 1 mm.

The Thickness Dependence of Response Speed in BNA-α Crystal.

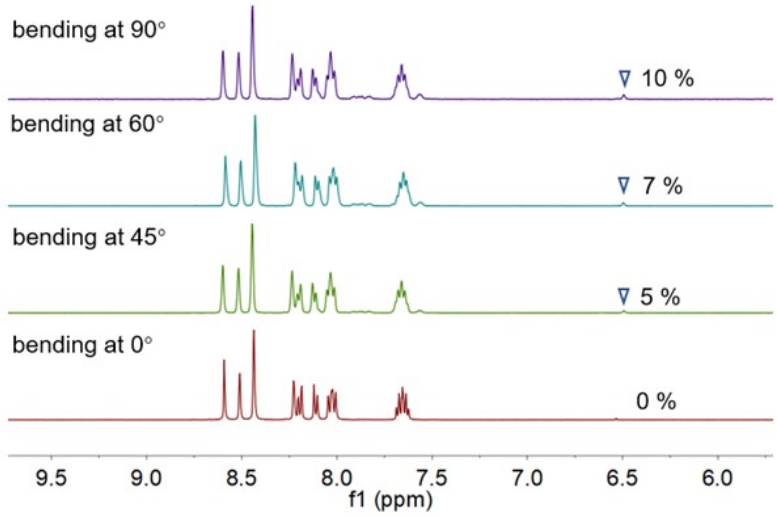

Figure S29. ^{1}H NMR spectrum of **BNA-α** crystals bending at 45°, 60° and 90° with the photodimerization of 5%, 7% and 10%, respectively.

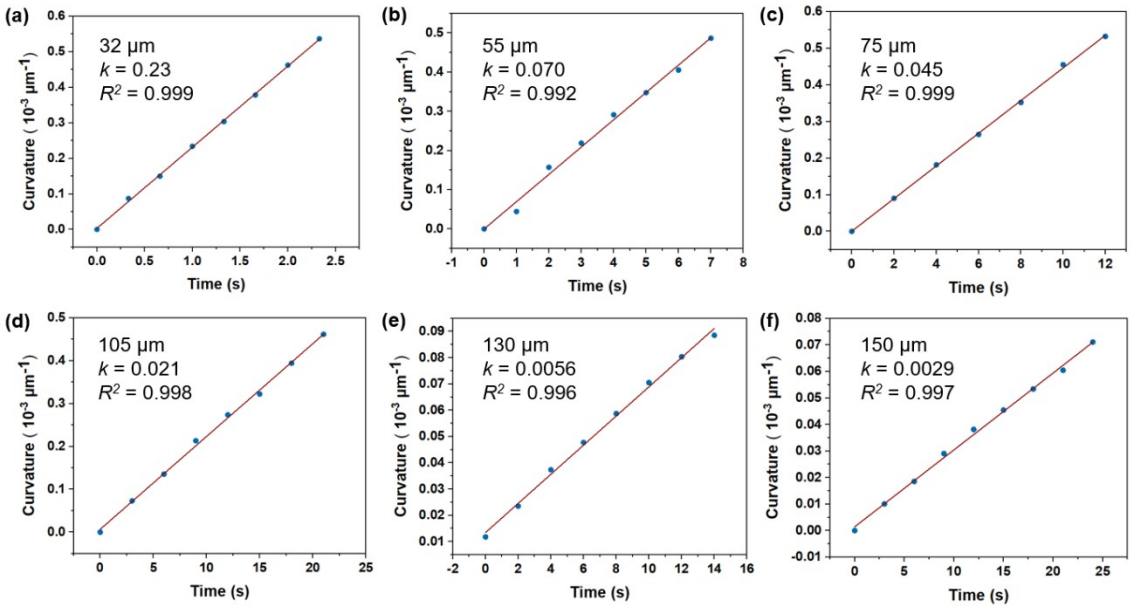

Figure S30. The bending responsive characteristics of **BNA-α** crystals with different thickness (from 30 to 150 μm) upon UV irradiation for different time. Dependence of the crystal curvature under continuous irradiation used to calculate the response rate (k) of curvature by the linear fit.

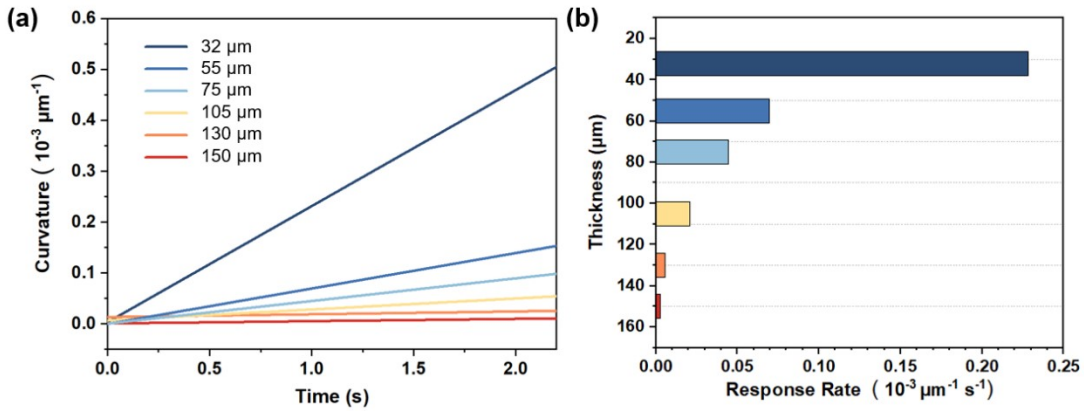

Figure S31. Thickness-dependent crystal deformation. (a) Dependence of the crystal curvature on irradiated time at different thicknesses. (b) Response rate of different thicknesses obtained from the linear fit of the curvature data.

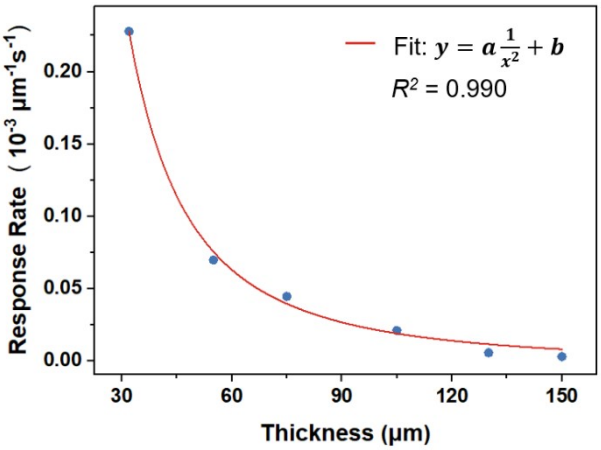

Figure S32. Dependence of the response on the crystal thickness. By fitting the data, we obtained a model, $y = a/x^2+b$, where x is the thicknesses of crystals, y is the response rate of curvature.

Photochromism Behaviors of BNA-α and BNA-β.

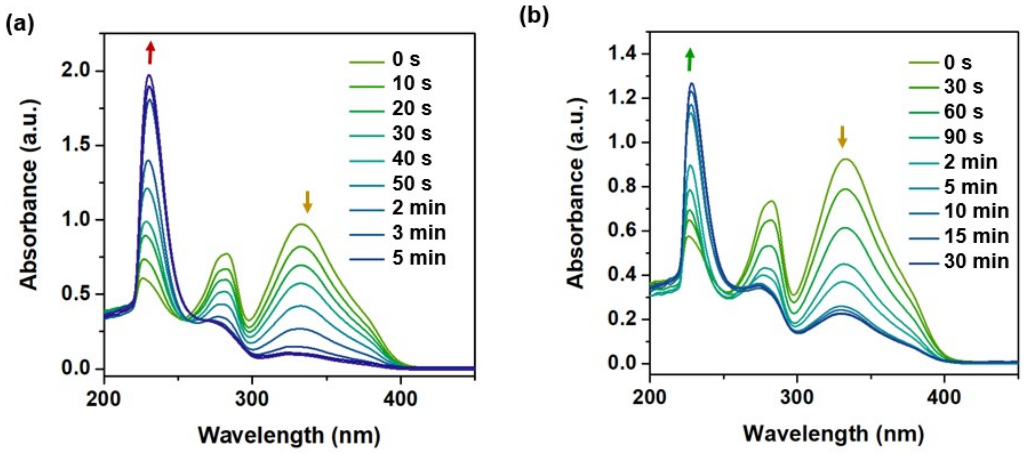

Figure S33. UV-vis absorption spectra of (a) **BNA-α** and (b) **BNA-β** at different UV irradiation time.

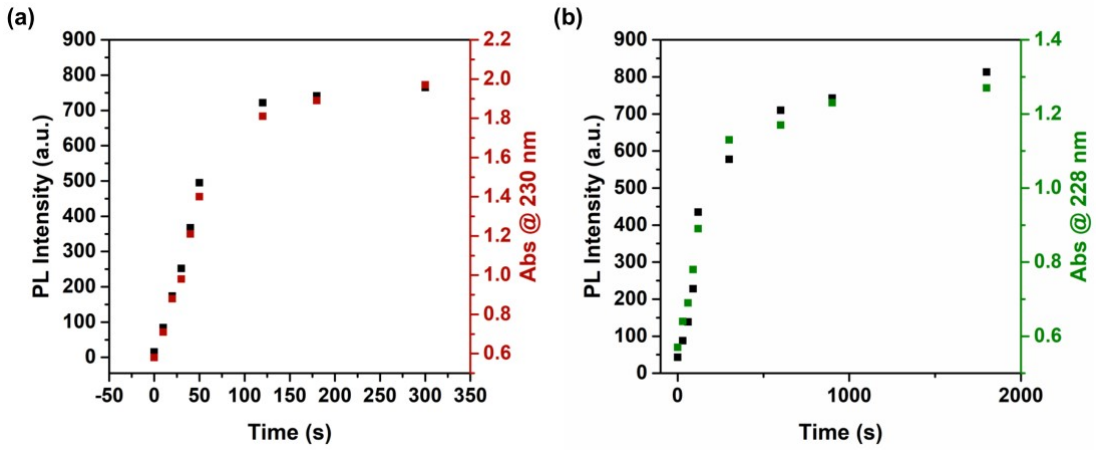

Figure S34. UV irradiant time-dependent profile of UV absorption intensity and the PL intensity of (a) **BNA-α** and (b) **BNA-β**.

The Mechanism of Fluorescence Change under UV Irradiation.

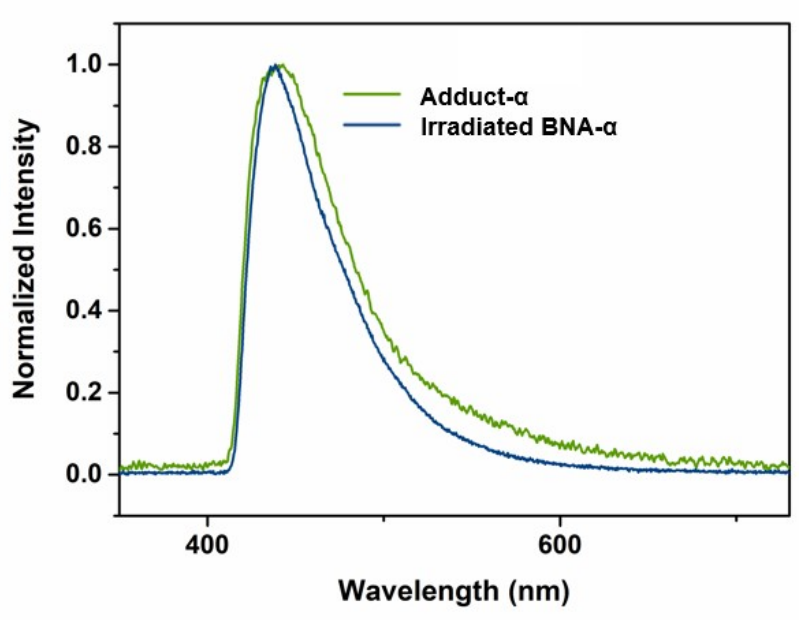

Figure S35. PL spectra of irradiated **BNA-α** (blue line) and **Adduct-α** (green line).

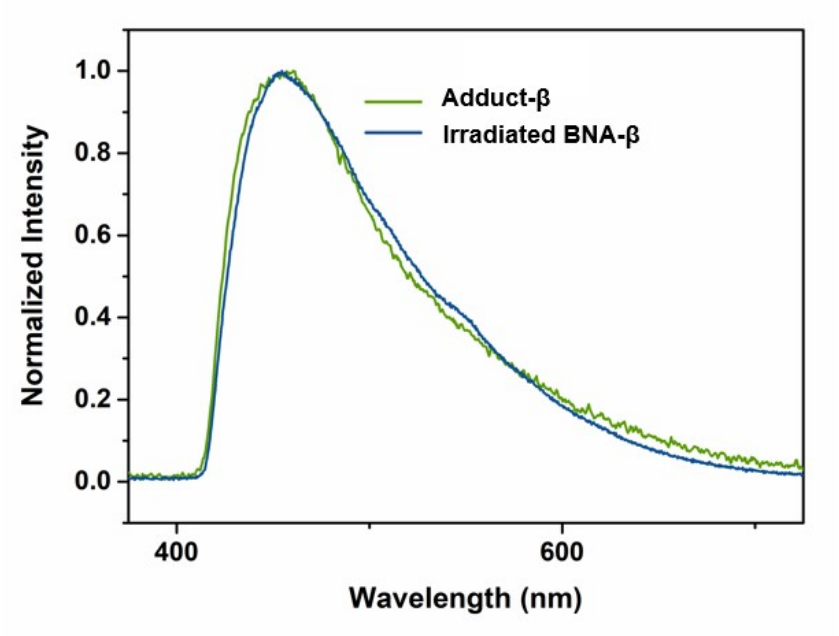

Figure S36. PL spectra of irradiate **BNA-β** (blue line) and **Adduct-β** (green line).

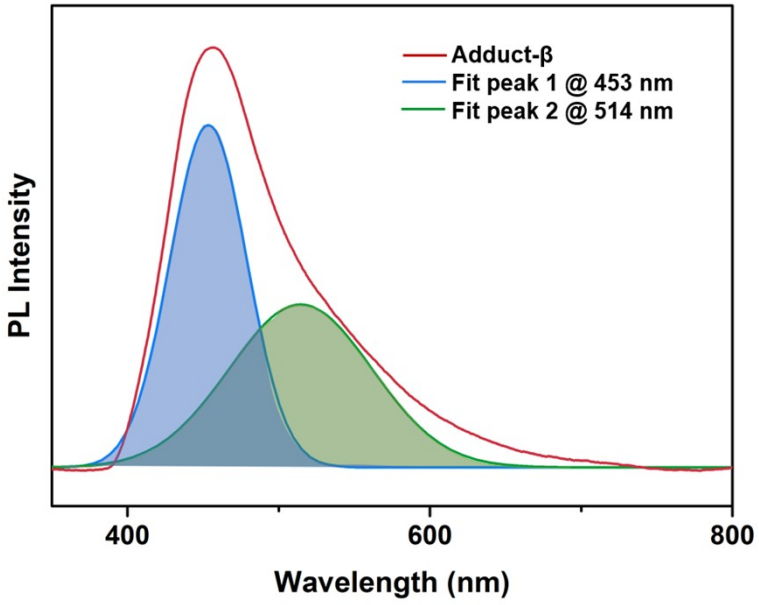

Figure S37. PL spectrum and fit peaks of **Adduct-β**.

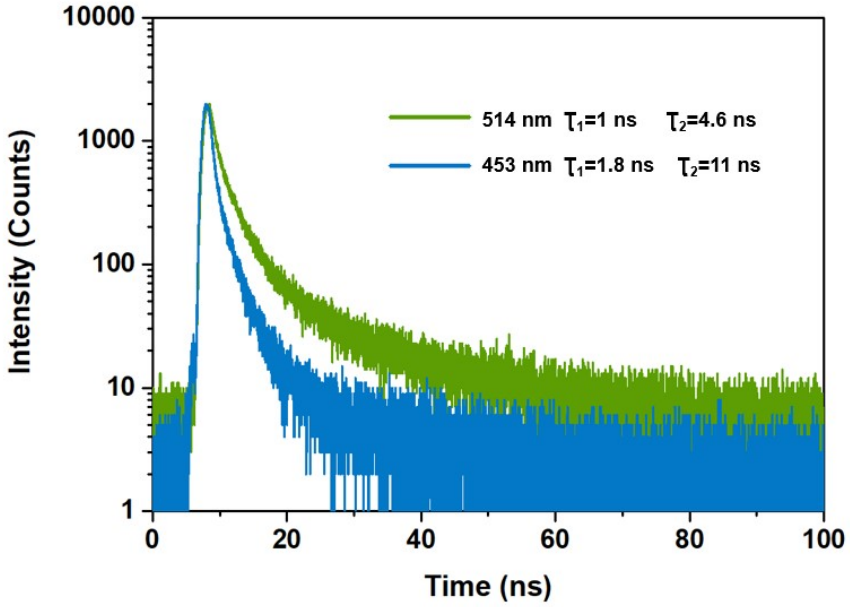

Figure S38. The fluorescence decay profiles of **Adduct-β** at 453 nm and 514 nm related to S_2 state and S_1 state shown the different average fluorescence lifetime, which further confirm the dual-state emission of **Adduct-β**.

The Photochromism Process of Rewritable Fluorescent Paper.

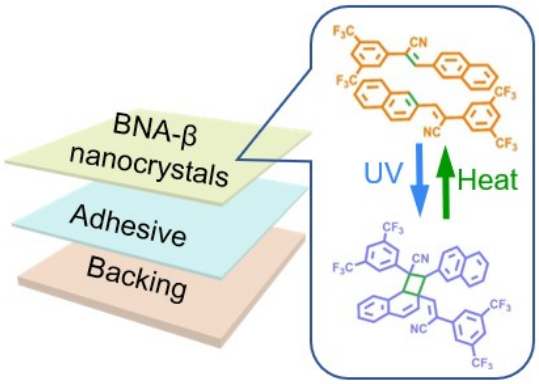

Figure S39. Fabrication of rewritable fluorescent paper based on **BNA-β** nanocrystals.

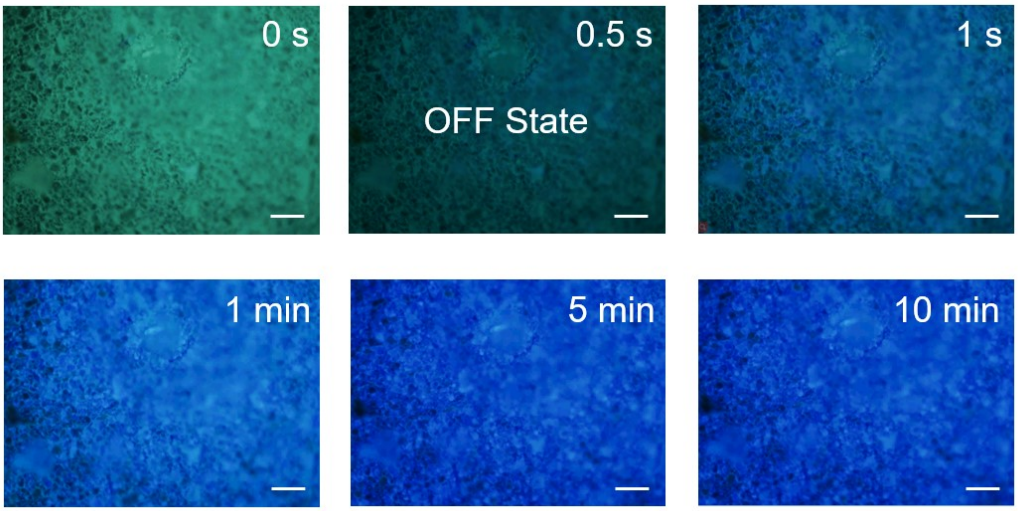

Figure S40. Fluorescence micrographs of **BNA-β** nanocrystals in rewritable fluorescent paper for different UV irradiation time. The scale bar is 20 μm.

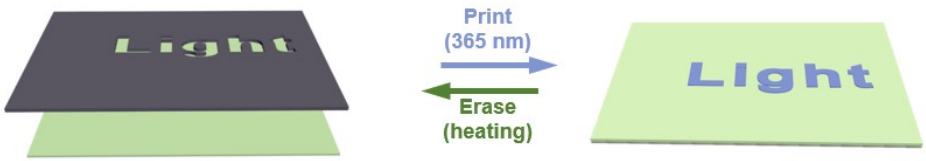

Figure S41. The printing process of rewritable fluorescent paper.

Supplementary Videos

Supplementary Video 1. This video showed the photoinduced bending process of **BNA-α** crystal.

Supplementary Video 2. This video showed the rapid fluorescence change of **BNA-β** nanocrystal in rewritable fluorescent paper, when we wrote with a laser pen and erased by heating at 90℃.